

Synthesis, crystal structure and superconductivity in $\text{RbLn}_2\text{Fe}_4\text{As}_4\text{O}_2$ ($Ln = \text{Sm, Tb, Dy and Ho}$)

Zhi-Cheng Wang,[†] Chao-Yang He,[†] Si-Qi Wu,[†] Zhang-Tu Tang,[†] Yi Liu,[†] and
Guang-Han Cao^{*,†,‡,¶}

[†]*Department of Physics, Zhejiang University, Hangzhou 310027, China*

[‡]*State Key Lab of Silicon Materials, Zhejiang University, Hangzhou 310027, China*

[¶]*Collaborative Innovation Centre of Advanced Microstructures, Nanjing 210093, China*

E-mail: ghcao@zju.edu.cn

Abstract

We have synthesized four iron-based oxyarsenide superconductors $\text{RbLn}_2\text{Fe}_4\text{As}_4\text{O}_2$ ($Ln = \text{Sm, Tb, Dy and Ho}$) resulting from the intergrowth of RbFe_2As_2 and LnFeAsO . It is found that the lattice match between RbFe_2As_2 and LnFeAsO is crucial for the phase formation. The structural intergrowth leads to double asymmetric Fe_2As_2 layers that are separated by insulating Ln_2O_2 slabs. Consequently, the materials are intrinsically doped at a level of 0.25 holes/Fe-atom and, bulk superconductivity emerges at $T_c = 35.8, 34.7, 34.3$ and 33.8 K, respectively, for $Ln = \text{Sm, Tb, Dy and Ho}$. Investigation on the correlation between crystal structure and T_c suggests that interlayer couplings may play an additional role for optimization of superconductivity.

INTRODUCTION

Recent years have witnessed discoveries of many iron-based superconductors (IBS) crystallizing in several structure types.¹⁻³ The key structural unit for the emergence of superconductivity is the anti-fluorite-type Fe_2X_2 ($\text{X} = \text{As}, \text{Se}$) layers, with which the parent (undoped) compounds mostly appear to be spin-density-wave (SDW) semi-metals. Superconductivity is induced by suppressing the SDW ordering via a certain chemical doping that may either introduce additional electrons⁴ or holes,⁵ or “apply” chemical pressures.⁶ Nevertheless, there is an alternative route towards superconductivity as well, namely, the electron (or hole) carriers are introduced by an internal charge transfer in the material itself. Examples include self-electron-doped $\text{Sr}_2\text{VFeAsO}_3$ ⁷ and $\text{Ba}_2\text{Ti}_2\text{Fe}_2\text{As}_4\text{O}$.⁸ More recent examples are manifested by the 1144-type $\text{AkAeFe}_4\text{As}_4$ ($\text{Ak} = \text{K}, \text{Rb}, \text{Cs}$; $\text{Ae} = \text{Ca}, \text{Sr}, \text{Eu}$)⁹⁻¹² and 12442-type $\text{KCa}_2\text{Fe}_4\text{As}_4\text{F}_2$,¹³ both of which are self-hole-doped owing to charge homogenization.

We previously formulated a strategy of structural design for the exploration of new IBS,³ which helps to discover the $\text{KCa}_2\text{Fe}_4\text{As}_4\text{F}_2$ superconductor.¹³ $\text{KCa}_2\text{Fe}_4\text{As}_4\text{F}_2$ can be viewed as an intergrowth of 1111-type CaFeAsF and 122-type KFe_2As_2 , as shown on the right side of Fig. 1. The resulting crystal structure possesses double Fe_2As_2 layers that are separated by the insulating fluorite-type Ca_2F_2 slab, mimicking the case of double CuO_2 planes in cuprate superconductors. Note that the CaFeAsF slab is undoped, while the KFe_2As_2 block is heavily hole doped (0.5 holes/Fe-atom). As a result, the hybrid structure intrinsically bears hole doping at 25%, which leads to absence of SDW ordering and appearance of superconductivity at 33 K.¹³ Along this research line, we succeeded in synthesizing two additional quinary fluo-arsenides $\text{AkCa}_2\text{Fe}_4\text{As}_4\text{F}_2$ ($\text{Ak} = \text{Rb}$ and Cs) with $T_c = 30.5$ K and 28.2 K, respectively.¹⁴ Furthermore, we also obtained the first 12442-type oxyarsenide $\text{RbGd}_2\text{Fe}_4\text{As}_4\text{O}_2$ which superconducts at 35 K.¹⁵ Questions arise naturally: can 12442-type oxyarsenides be synthesized if Gd is replaced by any other lanthanide elements? How does T_c change with such element replacements? Whether or not the lanthanide magnetism influences the T_c ?

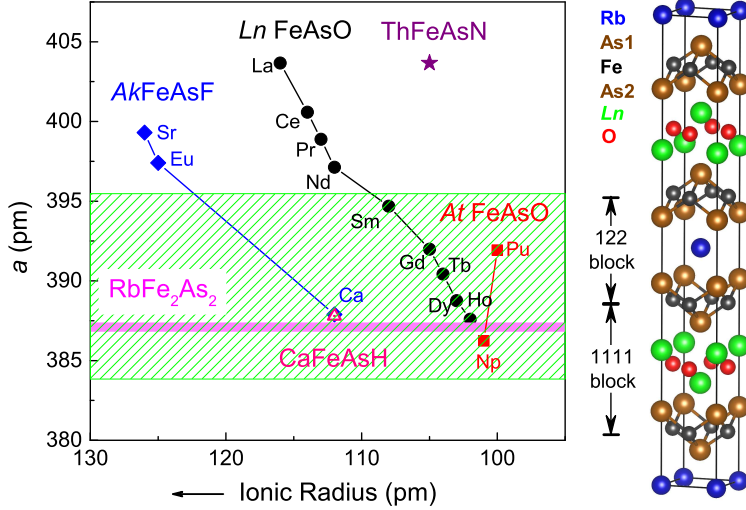


Figure 1: Lattice matching between 122-type RbFe_2As_2 and 1111-type LnFeAsO (Ln = lanthanide elements, data taken from Ref.¹⁶). Based on experimental results, the range for formation of $\text{RbLn}_2\text{Fe}_4\text{As}_4\text{O}_2$ is marked by the shaded area, where a good lattice match of RbFe_2As_2 and LnFeAsO is satisfied. The a parameters of CaFeAsH ,¹⁷ AeFeAsF ($\text{Ae} = \text{Ca}, \text{Sr}$ and Eu),^{18,19} AtFeAsO ($\text{At} = \text{Np}$ and Pu)^{20,21} and ThFeAsN ²² are put together for comparison. The horizontal axis denotes the ionic radii of Ae^{2+} [coordination number (CN) = 8], Ln^{3+} ($\text{CN} = 8$) and At^{3+} ($\text{CN} = 6$).²³ Shown at the right side is the 12442-type structure composed of 122- and 1111-blocks.

As we previously pointed out, lattice match between the constituent crystallographic block layers is crucial to realize the designed structures.³ So, let us first investigate the lattice-match issue. Fig. 1 plots lattice parameter a of various 1111-type Fe_2As_2 -layer containing compounds, in comparison with that of RbFe_2As_2 . The horizontal axis shows the effective ionic radii of Ae^{2+} , Ln^{3+} , At^{3+} ($\text{At} = \text{Np}$ and Pu) and Th^{4+} .²³ The data clearly explain why only Ca-containing fluo-arsenides $\text{AkCa}_2\text{Fe}_4\text{As}_4\text{F}_2$ were obtained (syntheses of $\text{AkAe}_2\text{Fe}_4\text{As}_4\text{F}_2$ with $\text{Ae} = \text{Sr}$ or Eu at ambient pressure were unsuccessful). Given the formation of $\text{RbGd}_2\text{Fe}_4\text{As}_4\text{O}_2$ at ambient pressure,¹⁵ one expects from the plot that synthesis of $\text{RbLn}_2\text{Fe}_4\text{As}_4\text{O}_2$ with $\text{Ln} = \text{Tb}$ and Dy is very likely (because of better lattice match). We actually succeeded in synthesizing four new members of $\text{RbLn}_2\text{Fe}_4\text{As}_4\text{O}_2$ with $\text{Ln} = \text{Sm}, \text{Tb}, \text{Dy}$ and Ho , among which $\text{RbHo}_2\text{Fe}_4\text{As}_4\text{O}_2$ is notable because the constituent HoFeAsO cannot be prepared at ambient pressure. In this paper, we report synthesis, crystal structure and superconductivity of the four new materials. Influences of crystal structure

and lanthanide magnetism on T_c are discussed.

EXPERIMENTAL SECTION

We attempted to synthesize seven target compounds $\text{RbLn}_2\text{Fe}_4\text{As}_4\text{O}_2$ with $Ln = \text{Nd, Sm, Tb, Dy, Ho, Er and Y}$, by employing a solid-state reaction method, similar to our previous report.¹³ The source materials include Rb ingot (99.75%), Ln ingot (99.9%), Ln_2O_3 and Tb_4O_7 powders (99.9%), Fe powders (99.998%) and As pieces (99.999%). Intermediate products of LnAs , FeAs and Fe_2As were presynthesized by direct solid-state reactions of their constituent elements. RbFe_2As_2 was additionally prepared by reacting Rb ingot (with an excess of 3%) and FeAs at 923 K for 10 hours. With these intermediate products, $\text{RbLn}_2\text{Fe}_4\text{As}_4\text{O}_2$ samples were finally synthesized by solid-state reactions of the stoichiometric mixtures of RbFe_2As_2 , LnAs , Ln_2O_3 , Tb_4O_7 , FeAs and Fe_2As . The chemical reactions take place in a small alumina container which is sealed in a Ta tube. The Ta tube was further jacketed with a quartz ampoule. This sample-loaded ampoule was sintered at 1213 - 1253 K for 40 hours, after which it was allowed to cool down by switching off the furnace.

Powder x-ray diffraction (XRD) was carried out on a PANalytical x-ray diffractometer with a $\text{CuK}_{\alpha 1}$ monochromator at room temperature. To obtain the crystallographic data of the new compounds $\text{RbLn}_2\text{Fe}_4\text{As}_4\text{O}_2$ with $Ln = \text{Nd, Sm, Tb, Dy and Ho}$, we made a Rietveld refinement employing the software RIETAN-FP.²⁴ The 12442-type structural model¹³ was adopted to fit the XRD data in the range of $20^\circ \leq 2\theta \leq 150^\circ$. The occupation factor of each atom was fixed to 1.0. As a result, the converged refinement yields fairly good reliable factors of $R_{\text{wp}} = 2.96\%$ ($Ln = \text{Sm}$), 2.98% ($Ln = \text{Tb}$), 2.46% ($Ln = \text{Dy}$) and 2.60% ($Ln = \text{Ho}$), and goodness-of-fit parameters of $S = 1.18$ ($Ln = \text{Sm}$), 1.01 ($Ln = \text{Tb}$), 1.14 ($Ln = \text{Dy}$) and 1.03 ($Ln = \text{Ho}$).

We employed a physical property measurement system (Quantum Design, PPMS-9) and a magnetic property measurement system (Quantum Design, MPMS-XL5) for the

measurements of temperature dependence of electrical resistance and magnetic moments. A standard four-electrode method and the ac transport option were utilized for the resistivity measurement. Samples for the magnetic measurements were cut into regular shape so that the demagnetization factors can be accurately estimated. To detect superconducting transitions, we applied a low field of 10 Oe in both zero-field cooling (ZFC) and field cooling (FC) modes. The isothermal magnetization curves above and well below T_c were measured. We also measured the temperature dependence of magnetic susceptibility up to room temperature under an applied field of 5000 Oe.

RESULTS AND DISCUSSION

Our XRD experiments indicate that the expected 12442-type $\text{RbLn}_2\text{Fe}_4\text{As}_4\text{O}_2$ can be successfully synthesized at ambient pressure for $Ln = \text{Sm, Tb, Dy}$ and Ho . In the case of $Ln = \text{Nd}$, however, only RbFe_2As_2 and NdFeAsO show up in the final product. This fact suggests that the lattice mismatch between RbFe_2As_2 and NdFeAsO , as shown in Fig. 1, is so heavy that $\text{RbNd}_2\text{Fe}_4\text{As}_4\text{O}_2$ is no longer stable at the ambient-pressure synthesis condition. From this empirical result, the criterion for possible formation of 12442-type phases is that the lattice mismatch, defined as $2(a_{1111} - a_{122})/(a_{1111} + a_{122})$, is less than 2%. For $Ln = \text{Er (Y)}$, the resulting phases are RbFe_2As_2 , Er_2O_3 (Y_2O_3), ErAs (YAs), Fe_2As and FeAs , although good lattice match between RbFe_2As_2 and “ ErFeAsO ” is expected (from extrapolation). The failure of synthesis of $\text{RbEr}_2\text{Fe}_4\text{As}_4\text{O}_2$ ($\text{RbY}_2\text{Fe}_4\text{As}_4\text{O}_2$) is then mainly due to the instability of the ErFeAsO (YFeAsO) block. For this reason, the successful synthesis of $\text{RbHo}_2\text{Fe}_4\text{As}_4\text{O}_2$ is remarkable, because HoFeAsO by itself cannot be synthesized at ambient pressure. Interestingly we sometimes observe HoFeAsO as a secondary phase when synthesizing $\text{RbHo}_2\text{Fe}_4\text{As}_4\text{O}_2$. This HoFeAsO phase could form as a result of decomposition of $\text{RbHo}_2\text{Fe}_4\text{As}_4\text{O}_2$ during the high-temperature solid-state reactions.

Given that NpFeAsO ²⁰ and PuFeAsO ²¹ can be synthesized at ambient pressure and, their

lattices well match that of RbFe_2As_2 (see Fig. 1), syntheses of $\text{RbAt}_2\text{Fe}_4\text{As}_4\text{O}_2$ ($At = \text{Np}$ and Pu) are very likely. It is of particular interest whether these 12442 species superconduct or not, since superconductivity is absent in the actinide-containing 1111 systems.²⁵ Noted also is the lattice match for CaFeAsH ¹⁷ (though it was synthesized at high pressures), as such, $\text{RbCa}_2\text{Fe}_4\text{As}_4\text{H}_2$ is also expectable. By employing high-pressure synthesis technique, additional 12442 members such as $\text{RbNd}_2\text{Fe}_4\text{As}_4\text{O}_2$ and $\text{RbY}_2\text{Fe}_4\text{As}_4\text{O}_2$ might also be synthesized. Furthermore, one may extend the synthesis to K- and Cs-containing 12442 series, similarly by the consideration of lattice match between KFe_2As_2 (or CsFe_2As_2) and LnFeAsO . Such studies are under going.

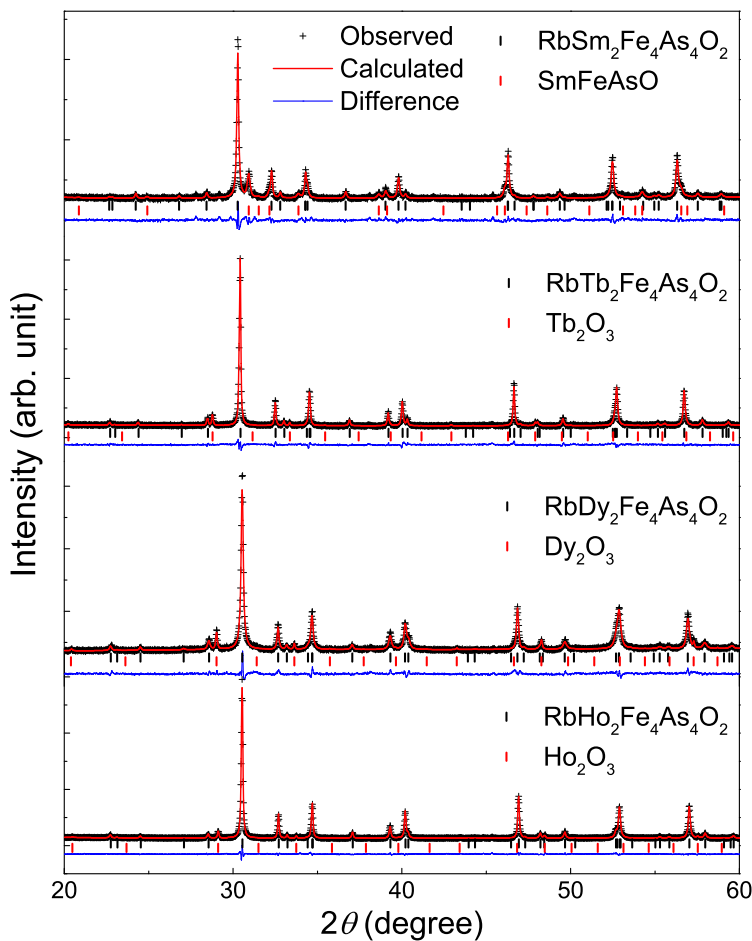


Figure 2: Powder X-ray diffraction patterns and their Rietveld refinement profiles for $\text{RbLn}_2\text{Fe}_4\text{As}_4\text{O}_2$ ($Ln = \text{Sm}, \text{Tb}, \text{Dy}$ and Ho). Only low-angle ($20^\circ \leq 2\theta \leq 60^\circ$) data are shown to highlight the main reflections.

Figure 2 shows the XRD patterns of $\text{RbLn}_2\text{Fe}_4\text{As}_4\text{O}_2$ with $Ln = \text{Sm, Tb, Dy}$ and Ho . Most of the reflections can be indexed with a body-centered tetragonal lattice of $a \approx 3.90 \text{ \AA}$ and $c \approx 31.3 \text{ \AA}$, consistent with the 12442-type structure.¹³ Samples of $Ln = \text{Tb, Dy}$ and Ho are nearly single phase. The detectable impurity is Ln_2O_3 whose weight percentages are 3.6 %, 3.9 % and 2.8 %, respectively, according to our Rietveld analyses. For $Ln = \text{Sm}$, synthesis of high-purity sample is difficult (the proportion of the main secondary phase SmFeAsO is 16.4 wt.% for the sample reported here). This might reflect that $\text{RbSm}_2\text{Fe}_4\text{As}_4\text{O}_2$ locates at the verge of chemical instability. The structural refinement results are listed in Table 1 where the data of $\text{RbGd}_2\text{Fe}_4\text{As}_4\text{O}_2$ ¹⁵ is also included for comparison.

Table 1: Room-temperature crystallographic data of $\text{RbLn}_2\text{Fe}_4\text{As}_4\text{O}_2$ in comparison with each other. The space group is $I4/mmm$ (No. 139). The atomic coordinates are as follows: $\text{Rb } 2a(0, 0, 0)$; $Ln 4e(0.5, 0.5, z)$; $\text{Fe } 8g(0.5, 0, z)$; $\text{As1 } 4e(0.5, 0.5, z)$; $\text{As2 } 4e(0, 0, z)$; $\text{O } 4d(0.5, 0, 0.25)$.

Ln	Sm	Gd (Ref. ¹⁵)	Tb	Dy	Ho
Lattice Parameters					
a (Å)	3.9209(2)	3.9014(2)	3.8900(1)	3.8785(2)	3.8688(1)
c (Å)	31.381(2)	31.343(2)	31.277(1)	31.265(2)	31.2424(7)
V (Å ³)	482.44(5)	477.06(4)	473.29(3)	470.30(4)	467.64(2)
Coordinates (z)					
Ln	0.2127(1)	0.2138(1)	0.21394(8)	0.21382(9)	0.21414(6)
Fe	0.1131(2)	0.1138(2)	0.11461(12)	0.11525(12)	0.11570(7)
As1	0.0707(2)	0.0697(2)	0.06990(14)	0.06907(17)	0.06961(8)
As2	0.1575(2)	0.1591(2)	0.15990(11)	0.15983(13)	0.16051(7)
Bond Distances					
Fe–As1 (Å)	2.369(5)	2.391(6)	2.396(3)	2.418(5)	2.412(2)
Fe–As2 (Å)	2.405(6)	2.413(6)	2.406(3)	2.388(3)	2.388(3)
As Height					
As1 (Å)	1.331(13)	1.382(13)	1.398(7)	1.444(10)	1.440(5)
As2 (Å)	1.387(13)	1.420(13)	1.417(7)	1.394(7)	1.400(7)
Bond Angles					
As1–Fe–As1 (°)	111.7(3)	109.4(3)	108.6(2)	106.6(2)	106.7(1)
As2–Fe–As2 (°)	109.2(3)	107.9(3)	107.9(2)	108.7(2)	108.2(1)
Fe_2As_2 -Layer Spacings					
d_{intra} (Å)	7.098(9)	7.134(10)	7.169(4)	7.207(5)	7.229(5)
d_{inter} (Å)	8.592(9)	8.538(10)	8.469(4)	8.426(5)	8.392(5)

Fig. 3 shows lattice parameters a and c of $\text{RbLn}_2\text{Fe}_4\text{As}_4\text{O}_2$ as a function of ionic radii of Ln^{3+} ($CN = 8$). Expectedly, both a and c axes decrease with decreasing the ionic radius. With careful examination, one sees that the cell parameters for $\text{Ln} = \text{Gd}$ are slightly larger than expected. This might be related to the half filling of $4f$ level for Gd^{3+} .

To investigate the lattice match effect, we also plot the average values of the constituent 122-type and 1111-type unit cells, i.e. $(a_{122} + a_{1111})/2$ and $c_{122} + 2c_{1111}$. Indeed, a and c basically meet the expected values of $(a_{122} + a_{1111})/2$ and $c_{122} + 2c_{1111}$, respectively. One expects that better lattice match would result in a more precise coincidence. However, the best coincidence is seen for $\text{Ln} = \text{Tb}$, albeit the lattice match is not the best (see Fig. 1). This can be explained by the charge homogenization which leads to an increase in a_{122} , and simultaneously, a decrease in a_{1111} . That is to say, the case of $\text{Ln} = \text{Tb}$ actually represents the best lattice match, provided the charge-transfer effect is taken into consideration. As shown in Table 1, indeed, the Fe–As1 and Fe–As2 bond distances (and other parameters including the As height and As–Fe–As bond angle) for $\text{Ln} = \text{Tb}$ are almost identical. Noted also is that the difference, $d_{\text{Fe–As1}} - d_{\text{Fe–As2}}$, tends to decrease, and changes its sign, from $\text{Ln} = \text{Sm}$ to $\text{Ln} = \text{Ho}$, which is in accordance with the data crossings at $\text{Ln} = \text{Tb}$ in Fig. 3.

Figure 4 shows resistivity data, $\rho(T)$, of the as-prepared $\text{RbLn}_2\text{Fe}_4\text{As}_4\text{O}_2$ ($\text{Ln} = \text{Sm}$, Tb , Dy and Ho) polycrystals. All the samples show a metallic behavior characterized by a round-shape dependence at around 150 K and a linear relation below ~ 75 K. The round-shape $\rho(T)$ behavior, which serves as a common characteristic of hole-doped IBS,^{5,13,26} is in contrast with the usual linear resistivity arising from electron-phonon scattering. The phenomenon could reflect an incoherent-to-coherent crossover that is in relation with an emergent Kondo-lattice effect.²⁷ The linear $\rho(T)$ behavior below 75 K is also different with those expected for electron-phonon and/or electron-electron scattering. It could represent a possible non-Fermi liquid behavior. The linearity stops when superconductivity sets in at $T_c^{\text{onset}} = 33.8 - 35.9$ K. The T_c^{onset} value decreases monotonically from $\text{Ln} = \text{Sm}$ to Tb , Dy and Ho (the variation of T_c on crystal structure and lanthanide magnetism will be further

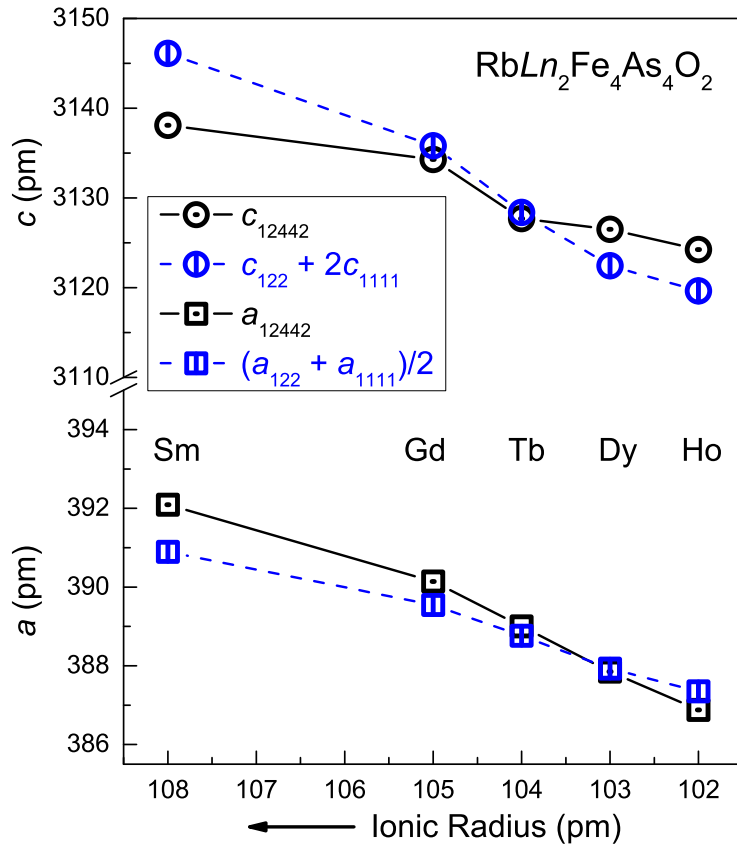


Figure 3: Lattice parameters of $\text{RbLn}_2\text{Fe}_4\text{As}_4\text{O}_2$ ($Ln = \text{Sm, Gd, Tb, Dy}$ and Ho) as a function of ionic radii of Ln^{3+} . The symbols in blue with dashed lines denote the average values of their constituent 122-type and 1111-type unit cells.

discussed later on). Coincidentally, the room-temperature resistivity and, the resistivity just above T_c in particular, decrease in the same manner. That is to say, T_c and the normal-state resistivity are positively correlated. If the resistivity is significantly contributed from non-phonon scatterings, as argued above, the correlation between T_c and the normal-state resistivity suggests a non-electron-phonon mechanism (such as spin-fluctuation mediated superconductivity) for the occurrence of superconductivity.

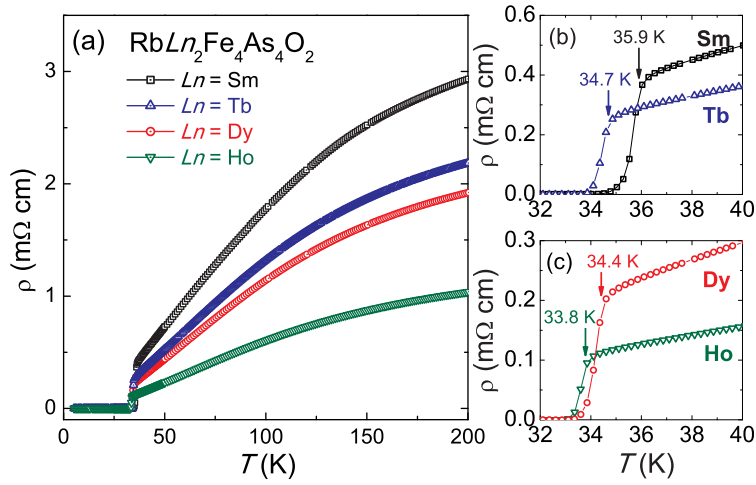


Figure 4: (a) Temperature dependence of resistivity for the $\text{RbLn}_2\text{Fe}_4\text{As}_4\text{O}_2$ ($\text{Ln} = \text{Sm}$, Tb , Dy and Ho) polycrystalline samples. Superconducting transitions are more clearly displayed in the right-side panels (b) and (c).

One of the striking properties in 12442-type superconductors is that the initial slope of upper critical field, $|\mu_0 dH_{c2}/dT|$, is exceptionally large among IBS.^{13–15} For example, the slope value for $\text{RbGd}_2\text{Fe}_4\text{As}_4\text{O}_2$ polycrystals achieves 16.5 T/K.¹⁵ To verify the commonality, we measured the magnetoresistance of a representative sample of $\text{RbHo}_2\text{Fe}_4\text{As}_4\text{O}_2$. As shown in Fig. 5, the superconducting onset transition shifts very mildly to lower temperatures under external magnetic fields, and simultaneously, the transition becomes significantly broadened with a long tail. To parameterize the field-dependent superconducting transitions, one may extract the upper critical field (H_{c2}) and the irreversible field (H_{irr}). Using the conventional criteria of 90% and 1% of the extrapolated normal-state resistivity, the transition temperatures as functions of H_{c2} and H_{irr} can be determined. The $H_{c2}(T)$ and $H_{\text{irr}}(T)$ data thus

derived are plotted in the inset of Fig. 5. One sees a steep $H_{c2}(T)$ line with a slope of 12.5 ± 0.6 T/K, which is significantly larger than other class of IBS including its relatives, 1144-type $\text{CaKFe}_4\text{As}_4$,²⁸ $\text{RbEuFe}_4\text{As}_4$ ¹¹ and $\text{CsEuFe}_4\text{As}_4$.¹²

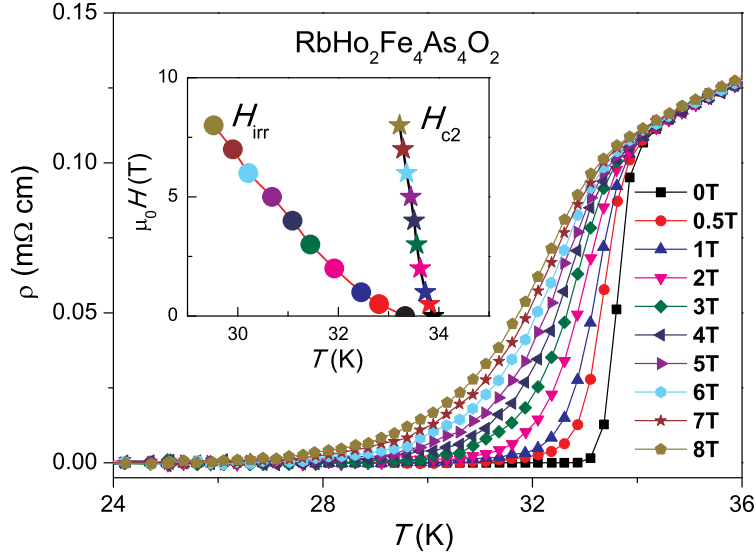


Figure 5: Superconducting resistive transitions under magnetic fields for the $\text{RbHo}_2\text{Fe}_4\text{As}_4\text{O}_2$ polycrystalline sample. The inset shows the extracted upper critical field H_{c2} and the irreversible field H_{irr} as a function of temperature.

Since the $|\mu_0 dH_{c2}/dT|$ value is proportional to the orbitally limited upper critical field at zero temperature, $H_{c2}^{\text{orb}}(0) \approx \frac{\Phi_0}{\xi_i \xi_j}$, where Φ_0 is the magnetic-flux quantum, ξ_i and ξ_j refer to the coherence lengths perpendicular to the field direction, one may immediately figure out that the coherence length, especially the one along the c axis, should be remarkably smaller than those of other class IBS. The short coherence length is probably originated from the enhanced two dimensionality in relation with the insulating spacer layers. Indeed, the large gap between $H_{c2}(T)$ and $H_{irr}(T)$ curves also dictates the weak interlayer coupling related to a short coherence length along the c axis.

Bulk superconductivity in $\text{RbLn}_2\text{Fe}_4\text{As}_4\text{O}_2$ is confirmed by the dc magnetic susceptibility shown in Fig. 6. Both ZFC and FC data show strong diamagnetism below the superconducting transitions. The onset transition temperatures are 35.8, 34.7, 34.3 and 33.8 K, respectively, for $Ln = \text{Sm}, \text{Tb}, \text{Dy}$ and Ho . The magnetic shielding volume fractions, i.e.

$4\pi\chi$ values in the ZFC mode, are all above 80% at 2 K. The magnetic repulsion fraction is greatly reduced to about 10%, which is due to magnetic-flux pinning effect. The flux pinning scenario is further demonstrated by the obvious magnetic hysteresis in the superconducting state (see insets of Fig. 6). One also notes that, apparently, there is a step-like anomaly below T_c in the ZFC data, which is absent for the FC data. This phenomenon is ascribed to the effect of intergrain weak links, which often appears for polycrystalline samples of extremely type-II superconductors.

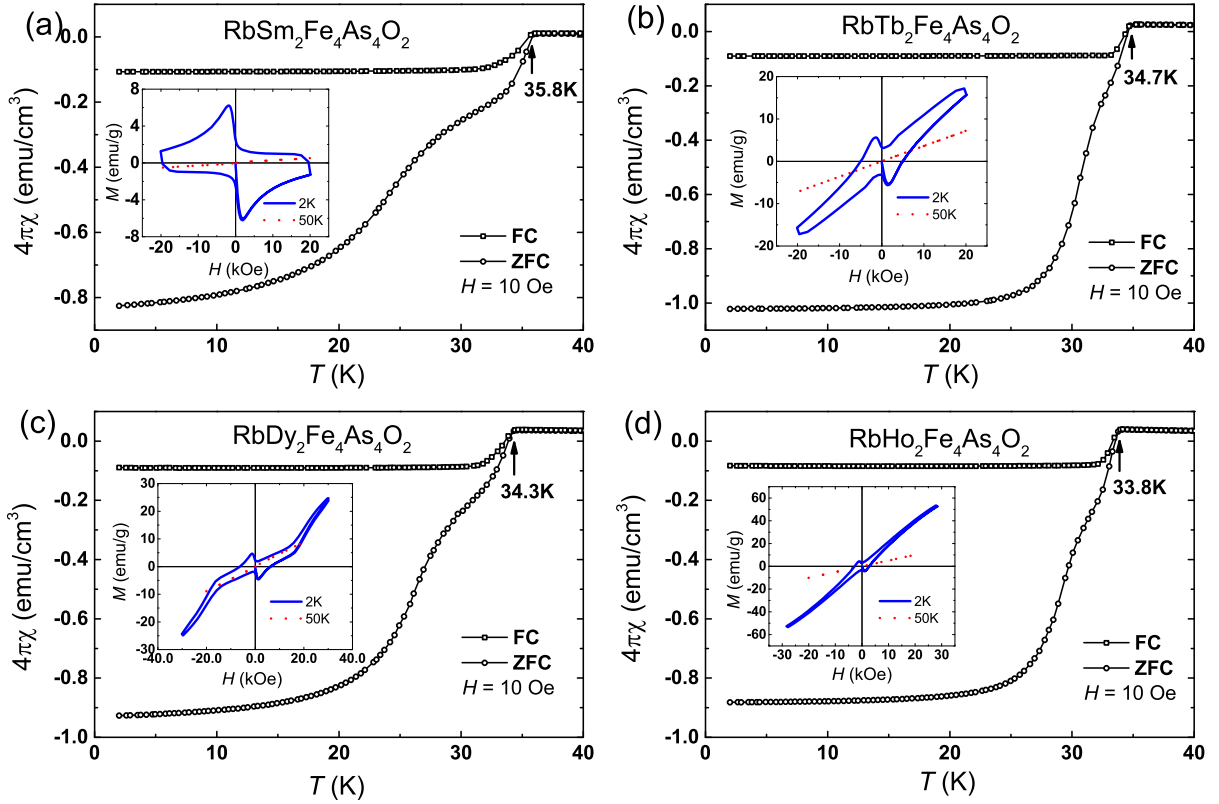


Figure 6: Superconductivity in $\text{RbLn}_2\text{Fe}_4\text{As}_4\text{O}_2$ ($Ln = \text{Sm}, \text{Tb}, \text{Dy}$ and Ho) evidenced by the dc magnetic susceptibility measured at $H = 10$ Oe in field-cooling (FC) and zero-field-cooling (ZFC) modes. Note that the data were corrected by removing the demagnetization effect. The insets show the isothermal magnetizations at 2 and 50 K.

The isothermal magnetization data, shown in the insets of Fig. 6, reflect the local-moment magnetism of Ln^{3+} as well. At 50 K (above T_c), the $M(H)$ relation is essentially linear with a slope (i.e. magnetic susceptibility) depending on Ln^{3+} . The magnetic susceptibility is dominantly contributed from the Curie-Weiss paramagnetism of Ln^{3+} moments. The

paramagnetic component is also evident in the superconducting state, as can be seen in the superconducting magnetic hysteresis at 2 K, especially for $Ln = \text{Tb, Dy and Ho}$. In the case of $Ln = \text{Dy}$, the magnetic hysteresis is superposed by a metamagnetic transition at about 20 kOe. Note that the Dy^{3+} magnetic moments in DyFeAsO become antiferromagnetically ordered below ~ 10 K.²⁹

To further investigate the local-moment magnetism of Ln^{3+} , we measured the normal-state magnetic susceptibility of $\text{RbLn}_2\text{Fe}_4\text{As}_4\text{O}_2$ with an applied field of 5 kOe, as displayed in Figs. 7. The local-moment paramagnetism is confirmed by the linearity in $1/\chi$. Then, one may be able to extract the effective magnetic moments of Ln^{3+} by a data fitting using the expression, $\chi = \chi_0 + C/(T - \theta_p)$, where χ_0 stands for the temperature-independent term, C is the Curie constant, and θ_p denotes the paramagnetic Curie temperature. To minimize the possible influence from crystal-field effect, we only fit the high-temperature data ($150 \text{ K} \leq T \leq 300 \text{ K}$). The fitting yields effective magnetic moments of 2.71, 9.85, 11.93, 10.46 μ_B/Ln -atom for $Ln = \text{Sm, Tb, Dy and Ho}$, respectively. The result basically meets the theoretical value of $g_J\sqrt{J(J+1)}$ (J is the quantum number of total angular momentum) for $Ln = \text{Tb, Dy and Ho}$. Note that the discrepancy for $Ln = \text{Sm}$ (the experimental value of effective moment is much bigger than the theoretical one) is frequently seen, which is due to low-lying excited states with different J from the ground states.³⁰

We found that the T_c value in $\text{RbLn}_2\text{Fe}_4\text{As}_4\text{O}_2$ remains unchanged (within ± 0.1 K), irrespective of sample's purity. This fact suggests that $\text{RbLn}_2\text{Fe}_4\text{As}_4\text{O}_2$ is a line compound which bears the same hole-doping level of 25%, similar to the case in 1144-type superconductors.⁹ Therefore, it is of meaning to study the possible factors that influence T_c . Fig. 8 shows T_c as a function of lattice constant a in $\text{RbLn}_2\text{Fe}_4\text{As}_4\text{O}_2$. One sees a monotonic increase of T_c with increasing a . Notably, however, the T_c value for $Ln = \text{Gd}$ is slightly lower than expected from the tendency. This anomaly could be caused by the Gd^{3+} magnetism which exhibits the biggest value of de Gennes factor, $(g_J - 1)^2 J(J + 1)$, as shown on the right axis in Fig. 8. The de Gennes factor measures the magnetic pair-breaking strength. Hence the

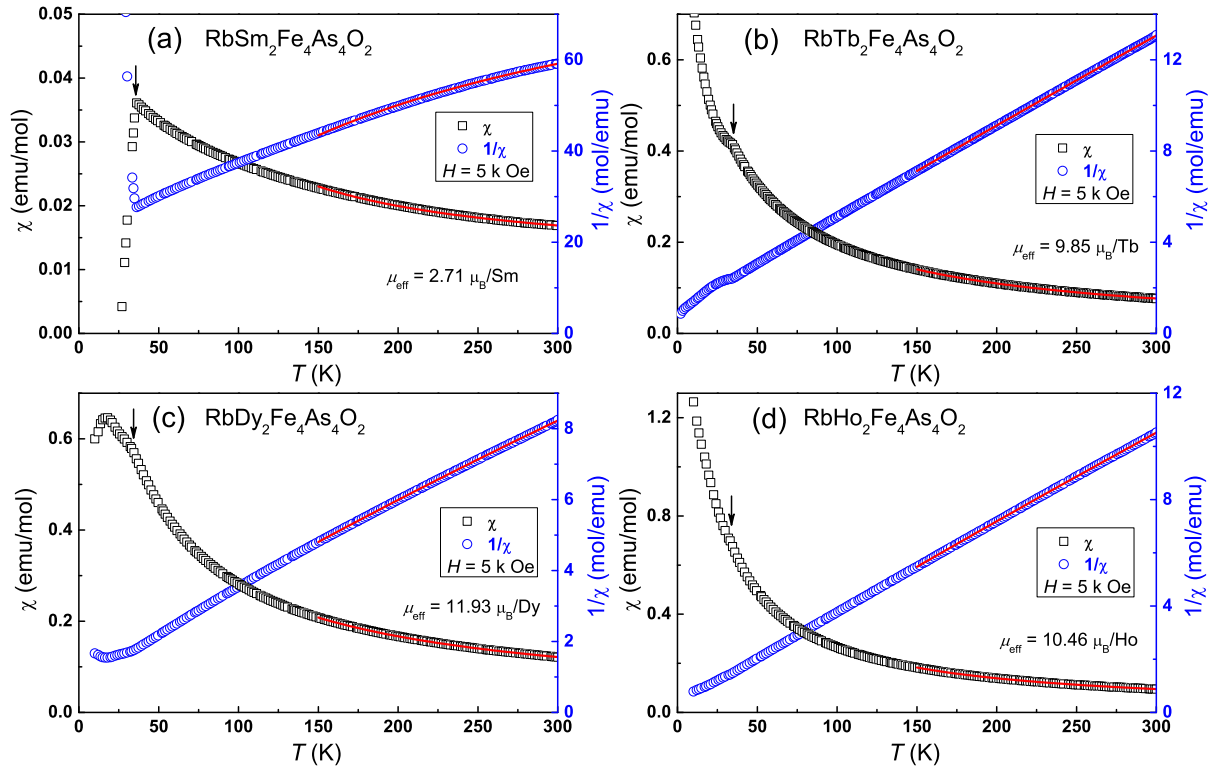


Figure 7: Temperature dependence of magnetic susceptibility in $\text{RbLn}_2\text{Fe}_4\text{As}_4\text{O}_2$ ($Ln = \text{Sm}, \text{Tb}, \text{Dy}$ and Ho). Superconducting transitions are marked by arrows. The right axis is used for showing the reciprocal of the susceptibility. The data between 150 and 300 K are fitted with Curie-Weiss law, from which the effective magnetic moments of Ln^{3+} are obtained.

slight decrease in T_c for $Ln = \text{Gd}$ actually dictates that Ln^{3+} magnetism hardly influence the T_c in $\text{RbLn}_2\text{Fe}_4\text{As}_4\text{O}_2$.

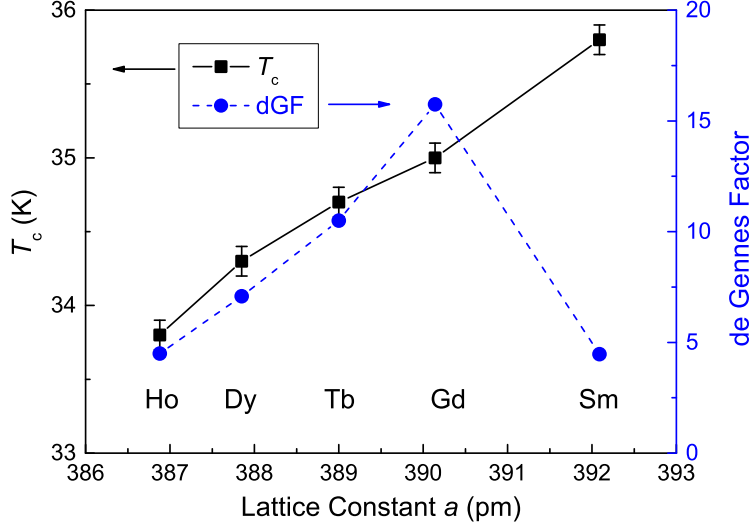


Figure 8: Lattice constant a vs. T_c (left axis) and de Gennes factor (right axis) in $\text{RbLn}_2\text{Fe}_4\text{As}_4\text{O}_2$ ($Ln = \text{Sm}, \text{Gd}, \text{Tb}, \text{Dy}$ and Ho).

The lattice-size dependence of T_c above contradicts with the case in $Ak\text{Ca}_2\text{Fe}_4\text{As}_4\text{F}_2$ ($Ak = \text{K}, \text{Rb}$ and Cs).¹⁴ Therefore, lattice constants are not good parameters that control T_c . In the $Ak\text{Ca}_2\text{Fe}_4\text{As}_4\text{F}_2$ series, we found that the spacings of Fe_2As_2 layers seem to be relevant: T_c increases with the decrease (increase) of intra(inter)-bilayer spacing, d_{intra} (d_{inter}). Note that d_{intra} and d_{inter} also measure the thickness of the 122- and 1111-like blocks, respectively (see Fig. 1). For $\text{RbLn}_2\text{Fe}_4\text{As}_4\text{O}_2$, a similar relation appears, as shown in Fig. 9(a). The slight deviation for $Ln = \text{Gd}$ could be due to the large de Gennes factor of Gd^{3+} as mentioned above. The observation of relationship between Fe_2As_2 -layer spacings and T_c suggests the role of interlayer coupling on superconductivity.

As far as a single Fe_2As_2 layer is concerned, in fact, the structural correlations of T_c are widely discussed in terms of the As–Fe–As bond angle, α , and/or the As height from the Fe plane, h_{As} .^{31–33} It is concluded that the maximum T_c appears at $\alpha = 109.5^\circ$ or $h_{\text{As}} = 138$ pm. As for $\text{RbLn}_2\text{Fe}_4\text{As}_4\text{O}_2$, we have two distinct As sites, which give two values for each parameter. It turns out that the difference in α or h_{As} does not correlate with T_c . We

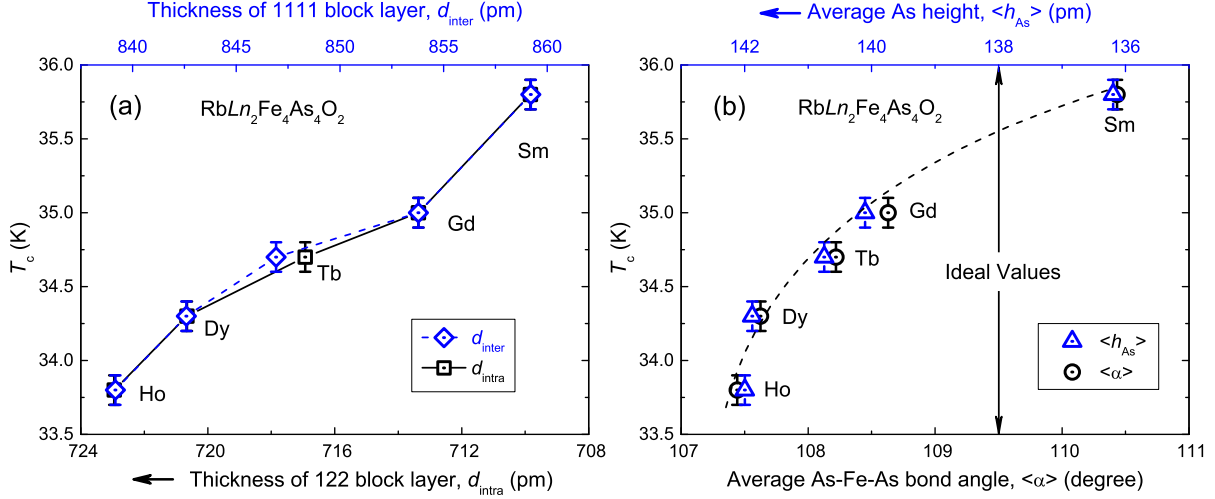


Figure 9: (a) T_c vs. thicknesses of the 122- and 1111-like blocks in $\text{RbLn}_2\text{Fe}_4\text{As}_4\text{O}_2$ ($Ln = \text{Sm, Gd, Tb, Dy}$ and Ho). (b) Influence of the average As–Fe–As bond angle and the As height from the Fe plane on T_c . The dashed line is a guide to the eye. The vertical line with arrows represents the values that are assumed to give the maximum T_c .

thus consider the average values, $\langle \alpha \rangle$ and $\langle h_{\text{As}} \rangle$ (this is reasonable because there is only one Fe site). Strikingly, a monotonic relation is found for both $\langle \alpha \rangle$ and $\langle h_{\text{As}} \rangle$, as shown in Fig. 9(b). No signature of T_c optimization is evident at $\alpha = 109.5^\circ$ or $h_{\text{As}} = 138$ pm. Invalidation of the correlations between T_c and the geometry of single Fe_2As_2 layer is also seen in $\text{AkCa}_2\text{Fe}_4\text{As}_4\text{F}_2$ system,¹⁴ which suggests that Fe_2As_2 -layer spacings could be another structural parameter controlling T_c .

CONCLUDING REMARKS

To summarize, we were able to synthesize the quinary $\text{RbLn}_2\text{Fe}_4\text{As}_4\text{O}_2$ series at ambient pressure for $Ln = \text{Sm, Tb, Dy}$ and Ho . The results indicate that lattice match between RbFe_2As_2 and LnFeAsO , which is modified by the charge homogenization, is crucial for the phase stabilization. In addition, the intergrowth constituents (such as LnFeAsO) themselves should preferably be stable. In this sense, formation of $\text{RbHo}_2\text{Fe}_4\text{As}_4\text{O}_2$ is remarkable because HoFeAsO cannot be synthesized in the stoichiometric composition at atmospheric pressure. According to the lattice-match viewpoint, we prospect that $\text{RbAt}_2\text{Fe}_4\text{As}_4\text{O}_2$ (At

= Np and Pu) and $AkLn_2Fe_4As_4O_2$ ($Ak = K$ and Cs) are likely to be synthesized for the future.

Like their sister materials, $RbLn_2Fe_4As_4O_2$ are featured by double asymmetric Fe_2As_2 layers that are intrinsically hole doped (0.25 holes/Fe-atom). Bulk superconductivity, instead of SDW order, appears in all the stoichiometric quinary compounds. The T_c values (from 33.8 to 35.8 K) are higher than those of 1111-type hole-doped superconductors which contain single separate single Fe_2As_2 layer, yet they are still lower than that of $(Ba,K)Fe_2As_2$ which contains infinite Fe_2As_2 layer. The widely accepted structural parameters related to T_c , i.e. As–Fe–As bond angle and As height from Fe plane, cannot account for the T_c variation. Instead, the Fe_2As_2 -layer spacing seems to be an important factor controlling T_c in 12442 systems. This suggests that interlayer couplings may play an additional role for optimization of superconductivity in IBS.

Acknowledgement

This work was supported by the National Science Foundation of China (Nos. 11474252 and 11190023) and the National Key Research and Development Program of China (No. 2016YFA0300202).

Supporting Information Available

The following files are available free of charge. CIF files of the crystallographic data of $RbLn_2Fe_4As_4O_2$ ($Ln = Sm, Gd, Tb, Dy$ and Ho).

References

- (1) Hosono, H.; Kuroki, K. *Phys. C* **2015**, *514*, 399–422.
- (2) Luo, X.; Chen, X. *Sci. China Mater.* **2015**, *58*, 77–89.

- (3) Jiang, H.; Sun, Y.-L.; Xu, Z.-A.; Cao, G.-H. *Chin. Phys. B* **2013**, *22*, 087410.
- (4) Kamihara, Y.; Watanabe, T.; Hirano, M.; Hosono, H. *J. Am. Chem. Soc.* **2008**, *130*, 3296–7297.
- (5) Wen, H.-H.; Mu, G.; Fang, L.; Yang, H.; Zhu, X. *EPL* **2008**, *82*, 17009.
- (6) Ren, Z.; Tao, Q.; Jiang, S.; Feng, C.; Wang, C.; Dai, J.; Cao, G.; Xu, Z. *Phys. Rev. Lett.* **2009**, *102*, 137002.
- (7) Cao, G.-H. et al. *Phys. Rev. B* **2010**, *82*, 104518.
- (8) Sun, Y. L.; Jiang, H.; Zhai, H. F.; Bao, J. K.; Jiao, W. H.; Tao, Q.; Shen, C. Y.; Zeng, Y. W.; Xu, Z. A.; Cao, G. H. *J. Am. Chem. Soc.* **2012**, *134*, 12893–12896.
- (9) Iyo, A.; Kawashima, K.; Kinjo, T.; Nishio, T.; Ishida, S.; Fujihisa, H.; Gotoh, Y.; Kihou, K.; Eisaki, H.; Yoshida, Y. *J. Am. Chem. Soc.* **2016**, *138*, 3410–3415.
- (10) Kawashima, K.; Kinjo, T.; Nishio, T.; Ishida, S.; Fujihisa, H.; Gotoh, Y.; Kihou, K.; Eisaki, H.; Yoshida, Y.; Iyo, A. *J. Phys. Soc. Jpn.* **2016**, *85*, 064710.
- (11) Liu, Y.; Liu, Y.-B.; Tang, Z.-T.; Jiang, H.; Wang, Z.-C.; Ablimit, A.; Jiao, W.-H.; Tao, Q.; Feng, C.-M.; Xu, Z.-A.; Cao, G.-H. *Phys. Rev. B* **2016**, *93*, 214503.
- (12) Liu, Y.; Liu, Y.-B.; Chen, Q.; Tang, Z.-T.; Jiao, W.-H.; Tao, Q.; Xu, Z.-A.; Cao, G.-H. *Sci. Bull.* **2016**, *61*, 1213–1220.
- (13) Wang, Z.-C.; He, C.-Y.; Wu, S.-Q.; Tang, Z.-T.; Liu, Y.; Ablimit, A.; Feng, C.-M.; Cao, G.-H. *J. Am. Chem. Soc.* **2016**, *138*, 7856–7859.
- (14) Wang, Z.-C.; He, C.-Y.; Tang, Z.-T.; Wu, S.-Q.; Cao, G.-H. *Sci. China Mater.* **2017**, *60*, 83–89.
- (15) Wang, Z.-C.; He, C.-Y.; Wu, S.-Q.; Tang, Z.-T.; Liu, Y.; Ablimit, A.; Tao, Q.; Feng, C.-M.; Xu, Z.-A.; Cao, G.-H. *J. Phys.: Condens. Matt.* **2017**, *29*, 11LT01.

- (16) Nitsche, F.; Jesche, A.; Hieckmann, E.; Doert, T.; Ruck, M. *Phys. Rev. B* **2010**, *82*, 134514.
- (17) Muraba, Y.; Matsuishi, S.; Hosono, H. *J. Phys. Soc. Jpn.* **2014**, *83*, 033705.
- (18) Matsuishi, S.; Inoue, Y.; Nomura, T.; Yanagi, H.; Hirano, M.; Hosono, H. *J. Am. Chem. Soc.* **2008**, *130*, 14428–14429.
- (19) Zhu, X. Y.; Han, F.; Cheng, P.; Mu, G.; Shen, B.; Zeng, B.; Wen, H. H. *Phys. C* **2009**, *469*, 381–384.
- (20) Klimczuk, T.; Walker, H. C.; Springell, R.; Shick, A. B.; Hill, A. H.; Gaczyński, P.; Gofryk, K.; Kimber, S. A. J.; Ritter, C.; Colineau, E.; Griveau, J.-C.; Bouëxière, D.; Eloirdi, R.; Cava, R. J.; Caciuffo, R. *Phys. Rev. B* **2012**, *85*, 174506.
- (21) Klimczuk, T.; Shick, A. B.; Springell, R.; Walker, H. C.; Hill, A. H.; Colineau, E.; Griveau, J.-C.; Bouëxière, D.; Eloirdi, R.; Caciuffo, R. *Phys. Rev. B* **2012**, *86*, 174510.
- (22) Wang, C.; Wang, Z.-C.; Mei, Y.-X.; Li, Y.-K.; Li, L.; Tang, Z.-T.; Liu, Y.; Zhang, P.; Zhai, H.-F.; Xu, Z.-A.; Cao, G.-H. *J. Am. Chem. Soc.* **2016**, *138*, 2170–2173.
- (23) Shannon, R. D. *Acta Crystallogr. Sect. A* **1976**, *32*, 751–767.
- (24) Izumi, F.; Momma, K. *Applied Crystallography XX*; Solid State Phenomena; Elsevier Ltd., 2007; Chapter 130, pp 15–20.
- (25) Walters, A. C.; Walker, H. C.; Springell, R.; Krisch, M.; Bosak, A.; Hill, A. H.; Zvoriste-Walters, C. E.; Colineau, E.; Griveau, J.-C.; Bouëxière, D.; Eloirdi, R.; Caciuffo, R.; Klimczuk, T. *J. Phys.: Condens. Matt.* **2015**, *27*, 325702.
- (26) Rotter, M.; Tegel, M.; Johrendt, D. *Phys. Rev. Lett.* **2008**, *101*, 107006.
- (27) Wu, Y. P.; Zhao, D.; Wang, A. F.; Wang, N. Z.; Xiang, Z. J.; Luo, X. G.; Wu, T.; Chen, X. H. *Phys. Rev. Lett.* **2016**, *116*, 147001.

- (28) Meier, W. R. et al. *Phys. Rev. B* **2016**, *94*, 064501.
- (29) Luo, Y.; Lin, X.; Li, Y.; Tao, Q.; Li, L.; Zhu, Z.; Cao, G.; Xu, Z. *Inter. J. Mod. Phys. B* **2012**, *26*, 1250207.
- (30) Blundell, S. *Magnetism in Condensed Matter*; Oxford University Press, Oxford, 2001; p 35.
- (31) Zhao, J.; Huang, Q.; de la Cruz, C.; Li, S.; Lynn, J. W.; Chen, Y.; Green, M. A.; Chen, G. F.; Li, G.; Li, Z.; Luo, J. L.; Wang, N. L.; Dai, P. *Nat. Mater.* **2008**, *7*, 953–959.
- (32) Lee, C.-H.; Iyo, A.; Eisaki, H.; Kito, H.; Fernandez-Diaz, M. T.; Ito, T.; Kihou, K.; Matsuhata, H.; Braden, M.; Yamada, K. *J. Phys. Soc. Jpn.* **2008**, *77*, 083704.
- (33) Mizuguchi, Y.; Hara, Y.; Deguchi, K.; Tsuda, S.; Yamaguchi, T.; Takeda, K.; Kotegawa, H.; Tou, H.; Takano, Y. *Supercond. Sci. Technol.* **2010**, *23*, 054013.